

# Depolarization ratio and attenuated backscatter for nine cloud types: analyses based on collocated CALIPSO lidar and MODIS measurements

Hyoun-Myoung Cho<sup>1</sup>, Ping Yang<sup>1\*</sup>, George W. Kattawar<sup>2</sup>, Shaima L. Nasiri<sup>1</sup>,  
Yongxiang Hu<sup>3</sup>, Patrick Minnis<sup>3</sup>, Charles Trepte<sup>3</sup>, David Winker<sup>3</sup>

<sup>1</sup>Department of Atmospheric Sciences, Texas A&M University, College Station, TX 77843

<sup>2</sup>Department of Physics, Texas A&M University, College Station, TX 77843

<sup>3</sup>NASA Langley Research Center, Hampton, VA 23681

\*Corresponding author: [pyang@ariel.met.tamu.edu](mailto:pyang@ariel.met.tamu.edu)

**Abstract:** This paper reports on the relationship between lidar backscatter and the corresponding depolarization ratio for nine types of cloud systems. The data used in this study are the lidar returns measured by the Cloud-Aerosol Lidar with Orthogonal Polarization (CALIOP) aboard the Cloud-Aerosol Lidar and Infrared Pathfinder Satellite Observations (CALIPSO) satellite and the collocated cloud products derived from the observations made by the Moderate Resolution Imaging Spectroradiometer (MODIS) aboard Aqua satellite. Specifically, the operational MODIS cloud optical thickness and cloud-top pressure products are used to classify cloud types on the basis of the International Satellite Cloud Climatology Project (ISCCP) cloud classification scheme. While the CALIPSO observations provide information for up to 10 cloud layers, in the present study only the uppermost clouds are considered. The layer-averaged attenuated backscatter ( $\gamma$ ) and layer-averaged depolarization ratio ( $\delta$ ) from the CALIPSO measurements show both water- and ice-phase features for global cirrus, cirrostratus, and deep convective cloud classes. Furthermore, we screen both the MODIS and CALIPSO data to eliminate cases in which CALIPSO detected two- or multi-layered clouds. It is shown that low  $\gamma$  values corresponding to uppermost thin clouds are largely eliminated in the CALIPSO  $\delta$ - $\gamma$  relationship for single-layered clouds. For mid-latitude and polar regions corresponding, respectively, to latitude belts 30°-60° and 60°-90° in both the hemispheres, a mixture of water and ice is also observed in the case of the altostratus class. MODIS cloud phase flags are also used to screen ice clouds. The resultant water clouds flagged by the MODIS algorithm show only water phase feature in the  $\delta$ - $\gamma$  relation observed by CALIOP; however, in the case of the ice clouds flagged by the MODIS algorithm, the co-existence of ice- and water-phase clouds is still observed in the CALIPSO  $\delta$ - $\gamma$  relationship.

©2008 Optical Society of America

OCIS codes: (010.3640) Lidar; (290.1090) Aerosol and cloud effects.

---

## References and links

1. D. M. Winker, J. Pelon, and M. P. McCormick, "The CALIPSO mission: Spaceborne lidar for observation of aerosols and clouds," *Proc. SPIE* **4893**, 1-11 (2003).
2. M. D. King, Y. J. Kaufman, W. P. Menzel, and D. Tanré, "Remote sensing of cloud, aerosol, and water vapor properties from the Moderate Resolution Imaging Spectrometer (MODIS)," *IEEE Trans. Geosci. Remote Sens.* **30**, 2-27 (1992).

3. B. A. Wielicki, E. F. Harrison, R. D. Cess, M. D. King, and D. A. Randall, "Mission to planet earth: Role of clouds and radiation in climate," *Bull. Am. Meteorol. Soc.* **76**, 2125-2153 (1995).
4. R. M. Schotland, K. Sassen, and R. Stone, "Observations by lidar of linear depolarization ratios by hydrometeors," *J. Appl. Meteor.* **10**, 1011-1017.
5. K. Sassen, "The polarization lidar technique for cloud research: A review and current assessment," *Bull. Am. Meteorol. Soc.* **72**, 1848-1866 (1991).
6. M. I. Mishchenko and K. Sassen, "Depolarization of lidar returns by small ice crystals: An application to contrails," *Geophys. Res. Lett.* **25**, 309-312 (1998).
7. Y. Hu, "Depolarization ratio-effective lidar ratio relation: Theoretical basis for space lidar cloud phase discrimination," *Geophys. Res. Lett.* **34**, doi:10.1029/2007/GL029584 (2007).
8. Y. Hu, M. Vaughan, Z. Liu, B. Lin, P. Yang, D. Flittner, B. Hunt, R. Kuehn, J. Huang, D. Wu, S. Rodier, K. Powell, C. Trepte, and D. Winker, "The depolarization - attenuated backscatter relation: CALIPSO lidar measurements vs. theory," *Opt. Express* **15**, 5327-5332 (2007).
9. W. B. Rossow and R. A. Schiffer, "Advances in understanding clouds from ISCCP," *Bull. Am. Meteorol. Soc.* **80**, 2261-2287 (1999).
10. M. D. King, W. P. Menzel, Y. J. Kaufman, D. Tanre, B.-C. Gao, S. Platnick, S. A. Ackerman, L. A. Remer, R. Pincus, and P. A. Hubanks, "Cloud and aerosol properties, precipitable water, and profiles of temperature and humidity from MODIS," *IEEE Trans. Geosci. Remote Sens.* **41**, 442-458 (2003).
11. S. Platnick, M. D. King, S. A. Ackerman, W. P. Menzel, B. A. Baum, J. C. Riédi, and R. A. Frey, "The MODIS cloud products: Algorithms and examples from Terra," *IEEE Trans. Geosci. Remote Sens.* **41**, 459-473 (2003).
12. W. P. Menzel, R. A. Frey, B. A. Baum, and H. Zhang, "Cloud top properties and cloud phase algorithm theoretical basis document," in MODIS Algorithm theoretical basis document pp. 55. (2006).
13. M. A. Vaughan, D. M. Winker, and K. A. Powell, "Part 2: Feature Detection and Layer Properties Algorithms," CALIOP Algorithm Theoretical Basis Document PC-SCI-202 Part 2, pp. 87 (2005).
14. Y. Hu, Z. Liu, D. Winker, M. Vaughan, and V. Noel, "Simple relation between lidar multiple scattering and depolarization for water clouds," *Opt. Lett.* **31**, 1809-1811 (2006).
15. K. Sassen and Y. Takano, "Parry arc: A polarization lidar, ray tracing, and aircraft case study," *Appl. Opt.* **39**, 6738-6745 (2000).
16. V. Noel and K. Sassen, "Study of ice crystal orientation in ice clouds from scanning polarization lidar observations," *J. Appl. Meteor.* **44**, 653-664 (2005).
17. K. Sassen, and S. Benson, "A midlatitude cirrus cloud climatology from the Facility for Atmospheric Remote Sensing: II. Microphysical properties derived from lidar depolarization," *J. Atmos. Sci.* **58**, 2103-2112 (2001).
18. H. Chepfer, G. Brogniez, P. Goloub, F. M. Breon, and P. H. Flamant, "Observations of horizontally oriented ice crystals in cirrus clouds with POLDER-1/ADEOS-1," *J. Quant. Spectrosc. Radiat. Transfer.* **63**, 521-543 (1999).
19. Y. You, G. W. Kattawar, P. Yang, Y. X. Hu, and B. A. Baum, "Sensitivity of depolarized lidar signals to cloud and aerosol particle properties," *J. Quant. Spectrosc. Radiat. Transfer.* **100**, 470-482 (2006).
20. A. J. Heymsfield, L. M. Miloshevich, A. Slingo, K. Sassen and D. O. Starr, "An observational and theoretical study of highly supercooled altocumulus," *J. Atmos. Sci.* **48**, 923-945 (1991).
21. P. R. Field, "Aircraft observations of ice crystal evolution in an altostratus cloud," *J. Atmos. Sci.* **56**, 1925-1941 (1999).
22. R. P. Fleishauer, V. E. Larson and T. H. Vonder Haar, "Observed microphysical structure of midlevel, mixed-phase clouds," *J. Atmos. Sci.* **59**(11), 1779-1804 (2002).
23. R. A. McClatchey, R. W. Fenn, J. E. A. Selby, F. E. Volz, and J. S. Garing, "Optical properties of the atmosphere," (third edition) AFCRL-72-0497, Air Force Cambridge Research Laboratories (1972).
24. C. M. Naud, B. A. Baum, M. Pavolonis, A. Heidinger, R. Frey, and H. Zhang, "Comparison of MISR and MODIS cloud-top heights in the presence of cloud overlap," *Remote Sens. Environ.* **107**, 200-210 (2007).
25. R. T. Marchand, T. P. Ackerman, and C. Moroney, "An assessment of Multiangle Imaging Spectroradiometer (MISR) stereo-derived cloud top heights and cloud top winds using ground-based radar, lidar, and microwave radiometers," *J. Geophys. Res.* **112**, D06204, doi:10.1029/2006JD007091 (2007).
26. E. Weisz, J. Li, W. P. Menzel, A. K. Heidinger, and B. H. Kahn, "Comparison of AIRS, MODIS, CloudSat and CALIPSO cloud top height retrievals," *Geophys. Res. Lett.* **34**, L17811 (2007).
27. G. M. McFarquar and A. J. Heymsfield, "Microphysical Characteristics of Three Anvils Sampled during the Central Equatorial Pacific Experiment," *J. Atmos. Sci.* **53**, 2401-2423 (1996).
28. A. J. Heymsfield, and J. Iaquinta, "Cirrus Crystal Terminal Velocities," *J. Atmos. Sci.* **57**, 916-938 (2000).
29. S. G. Cober, G. A. Isaac, A. V. Korolev, and J. W. Strapp, "Assessing cloud phase conditions," *J. Appl. Meteorol.* **40**, 1967-1764 (2001).

## 1. Introduction

Nearly simultaneous observations of clouds by active and passive sensors, made possible with instruments in the “A-train” constellation of satellites, offer unprecedented opportunities to study cloud systems from a global perspective. This paper focuses on combining an A-train active sensor, the Cloud-Aerosol Lidar with Orthogonal Polarization (CALIOP) on the Cloud-Aerosol Lidar and Infrared Pathfinder Satellite Observations (CALIPSO) [1] satellite, with a passive sensor, the Moderate Resolution Imaging Spectroradiometer (MODIS) [2] on the Aqua satellite to study relationships between cloud phase, cloud height, and cloud optical thickness. These three properties are important for monitoring cloud-climate feedbacks and comparing satellite observations with climate model outputs [3].

The CALIOP, referred to here as the CALIPSO lidar, operates at two channels centered at wavelengths 532 nm and 1064 nm [1]. A feature of the CALIPSO lidar 532-nm channel is dual polarization. Polarimetric lidar returns offer enhanced abilities for studying and differentiating atmospheric hydrometeors, as demonstrated by Schotland et al. [4], Sassen [5], and Mishchenko and Sassen [6]. For example, the relationship between lidar depolarization ratio and effective lidar ratio provides a powerful approach to determine cloud thermodynamic phase [7]. This paper focuses heavily on recent research by Hu et al. [7, 8] demonstrating how the relationship between lidar depolarization ratio and attenuated backscatter allows discrimination between cloud phases.

The relationship between the layer-integrated depolarization ratio ( $\delta$ ) and the layer-integrated attenuated backscatter ( $\gamma'$ ) measured by the CALIPSO lidar at 532 nm is investigated for nine types of cloud systems classified on the basis of the International Satellite Cloud Climatology Project (ISCCP) cloud classification scheme [9]. The MODIS-based retrievals of cloud height and optical thickness [10, 11] are used to classify cloud types. We also consider the cloud  $\delta$ - $\gamma'$  relation with respect to latitude and the cloud phases determined by the MODIS infrared cloud-phase algorithm [12] and the MODIS decision tree algorithm [11].

## 2. Data and method

The CALIPSO cloud products used in this study are the CALIPSO level-2 layer data with 1-km spatial resolution at the surface. The pitch angle of the CALIOP lidar for the data sets used here is within  $0.3^\circ$  from nadir. Specifically, we use the layer-integrated depolarization ratio ( $\delta$ ) and the total layer-integrated attenuated backscatter ( $\gamma'$ ) at 532 nm, which are defined as follows [8,13]:

$$\delta = \frac{\int_{top}^{base} \beta'_{\perp}(z) dz}{\int_{top}^{base} \beta'_{\parallel}(z) dz}, \quad (1)$$

$$\gamma' = \int_{top}^{base} [\beta'_{\parallel}(z) + \beta'_{\perp}(z)] dz, \quad (2)$$

where  $\beta'_{\perp}$  and  $\beta'_{\parallel}$  are the perpendicular and parallel components of the attenuated backscatter, respectively. While the CALIPSO data product contains information on up to 10 cloud layers within each 1 km retrieval footprint, this study uses only the uppermost cloud layer.

Hu et al. [8] derived the relationships between CALIPSO lidar  $\delta$  and  $\gamma'$  for both ice and water clouds, which are schematically depicted in Fig. 1. For water clouds consisting of spherical liquid droplets,  $\delta$  and  $\gamma'$  are positively correlated, whereas the correlations are negative for ice clouds. It should be pointed out that while the single scattering by water droplets does not depolarize the backscattered light, multiple scattering events within a water cloud do tend to depolarize lidar signals [14]. Therefore, the depolarization ratio associated with water clouds increases with increasing backscatter and is positively correlated to the

optical depth [7]. The curves for water and ice cross each other near  $\delta=0.171$  and  $\gamma=0.0623$ . The lower right portion of the ice cloud curve (below the intersection with the water curve), corresponding to depolarization ratios between 0.3 and 0.5, is associated with ice clouds consisting of randomly oriented ice particles. The upper left portion of the ice curve, corresponding to high backscatter and small depolarization ratio values, is associated with clouds consisting of horizontally oriented ice crystals such as plates [8], or horizontally oriented ice columns, such as Parry-oriented columns [15,16]. When the CALIOP lidar is pointed within  $0.3^\circ$  within nadir, the specular reflection caused by two horizontally-parallel faces of horizontally-oriented ice plates or Parry-oriented columns leads to large backscatter. The specular reflection in this case, however, does not depolarize the backscattered lidar beam because the parallel and perpendicular components of the electric vector associated with the lidar beam are indistinguishable with respect to a horizontal plane. The presence of horizontally-oriented ice crystals has been confirmed using ground-based lidar observations [16,17]. Additionally, Chepfer et al. [18], using satellite-based observations by the Polarization and Directionality of Earth Reflectances (POLDER) instrument, found horizontally oriented ice crystals in approximately 40% of ice clouds.

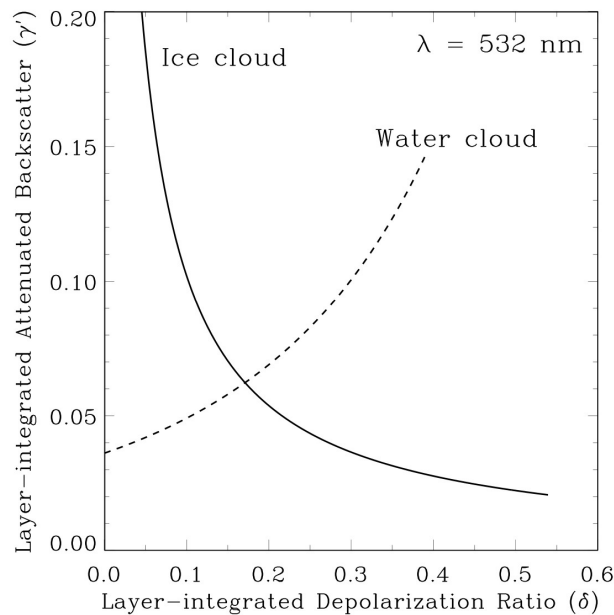


Fig. 1. Schematic curves showing the relationships (Hu et al. [8]) between the layer-integrated depolarization ratio and layer-integrated attenuated backscatter coefficient for ice clouds (solid line) and water clouds (dashed line).

The MODIS retrieved cloud properties used in the present study are Collection-5 MYD06 level-2 cloud products, specifically, optical thickness ( $\tau$ ), cloud top pressure ( $P_{top}$ ), cloud top temperature (CTT), and two cloud phase products [11]. The retrieval of  $\tau$  is accomplished using reflectances at  $2.1 \mu\text{m}$  and either  $0.65$ ,  $0.8$ , or  $1.2 \mu\text{m}$ , depending on surface type; the retrieved product resolution is  $1 \text{ km}$  by  $1 \text{ km}$ . The  $P_{top}$  retrievals utilize the  $\text{CO}_2$ -slicing method for high and midlevel clouds and  $11 \mu\text{m}$  brightness temperature matched to a numerical weather prediction model analysis vertical temperature profile for low clouds; the product resolution is  $5 \text{ km}$  by  $5 \text{ km}$ . The first MODIS cloud-phase product in this study is the operational bispectral infrared (IR) cloud phase algorithm [12]. It uses the brightness temperatures at two IR channels and classifies clouds as water-, ice-, or mixed- or uncertain-phase at  $5 \text{ km}$  resolution. The second cloud phase product uses a multitude of channels and is

used in the first step in the retrieval of cloud  $\tau$  and effective radius. This product is at 1 km resolution and is denoted here as the retrieval processing path (RPP) phase. Because the  $\tau$  and RPP phase retrievals rely on reflected solar radiation, all of our comparisons use only daytime MODIS and CALIPSO observations.

In terms of cloud top pressure and optical thickness, clouds are classified on the basis of the ISCCP scheme [9]. Specifically, a cloud is first categorized as high ( $50 \text{ hPa} < P_{top} < 440 \text{ hPa}$ ), middle ( $440 \text{ hPa} < P_{top} < 680 \text{ hPa}$ ), or low ( $680 \text{ hPa} < P_{top} < 1000 \text{ hPa}$ ). Each cloud-top pressure category is further categorized into one of three sub-types based on cloud optical thickness ( $\tau$ ). For example, high clouds consist of cirrus clouds ( $0 < \tau < 3.6$ ), cirrostratus clouds ( $3.6 < \tau < 23$ ), and deep convective clouds ( $23 < \tau < 379$ ). Similarly, middle clouds are categorized as altostratus, altostratus, and nimbostratus with respect to the three optical thickness ranges, whereas low clouds are categorized as cumulus, stratocumulus, and stratus. It should be stressed that these cloud classifications are based only on retrieved cloud top height and optical thickness, and therefore vary from other meteorological uses of the class categories.

### 3. CALIPSO lidar $\delta$ - $\gamma'$ relations for MODIS-based cloud classes

The CALIPSO lidar derived  $\delta$ - $\gamma'$  relations are shown for MODIS-based cloud classes. The data for these figures come from 12 months (July 2006 - June 2007) of collocated MODIS Level-2 MYD06 cloud products and CALIPSO Level-2 1-km cloud layer products. The collocation is based on matching the CALIPSO pixels to the nearest MODIS pixels for both 1 km and 5 km MODIS resolution. For those MODIS variables with a resolution of 5 km by 5 km, approximately 5 CALIPSO pixels correspond to the same MODIS properties. In each figure, the  $\delta$ - $\gamma'$  relation is plotted for each cloud class with color representing the number of occurrences for a  $\Delta\delta$ - $\Delta\gamma'$  box with 0.01 (for  $\Delta\delta$ ) by 0.002  $\text{sr}^{-1}$  (for  $\Delta\gamma'$ ) interval.

The  $\delta$ - $\gamma'$  relation for the uppermost layers over the entire 1 year dataset is shown in Fig. 2. In total, 4353 daytime CALIPSO granules are used in this study. At daytime, there are 14 to 15 CALIPSO granules per day. A daytime CALIPSO granule consists of approximately 21,000 pixels. The clusters of high observation occurrence match well to the water and ice cloud curves in Fig. 1. Note that the  $\delta$ - $\gamma'$  patterns for high clouds (cirrus, cirrostratus, and deep convection), altostratus, and nimbostratus are similar to those shown by Hu et al. [8] for the case where the CALIPSO lidar was pointed at  $0.3^\circ$  of nadir. All CALIPSO lidar data used in this study are pointed at  $0.3^\circ$  of nadir.

For the  $\delta$ - $\gamma'$  relationship for high clouds, the feature associated with randomly oriented ice crystals (i.e. low backscatter portion of each panel) dominates, particularly in the cirrus class. However, the feature associated with horizontally oriented crystals (i.e. upper left portion) is prominent for the mid to high optical thickness cases of cirrostratus, deep convection, altostratus, nimbostratus and stratocumulus. The layer-integrated attenuated backscatter values for thick clouds are larger than those for thin clouds because  $\gamma'$  is proportional to cloud thickness. However, the differences between the results for cirrostratus clouds and deep convection are smaller than the counterparts for cirrus and cirrostratus clouds. This feature is primarily due to the attenuation of backscatter within clouds. However, the depolarization ratio in the case of ice clouds consisting of randomly oriented ice crystals is not sensitive to optical depth. The variation of the depolarization ratio is primarily due to different ice crystal habits [19].

Figure 2 also shows clusters with the positive slope feature associated with water clouds in Fig. 1. This feature is dominant in the low cloud classes, implying, as expected, that these low clouds tend to be water-phase. However, signatures associated with both ice and water clouds are found in the midlevel (altostratus, in particular) and high cloud classes. These results are not surprising for the midlevel cloud classes, as *in situ* observations show that midlevel clouds can be composed of super-cooled liquid water droplets [20], ice crystals [21], or a mixture of both ice and water [22]. The water cloud signatures in the high cloud classes may be due to supercooled-water as the temperatures at 440 hPa in standard McClatchey et al.

[23] tropical and midlatitude summer atmospheres are between 258 and 256 K. For the highest cloud classes, though, we also have to consider the possibility of cloud height misclassification by MODIS, or horizontal inhomogeneities at smaller scales than the MODIS 5x5 km product resolution. If high ice clouds and low level water clouds both exist, not necessarily overlapping geometrically, within a 5 km x 5 km MODIS footprint, they may be assigned a high cloud height by MODIS, while CALIPSO may see individual water clouds and ice clouds.

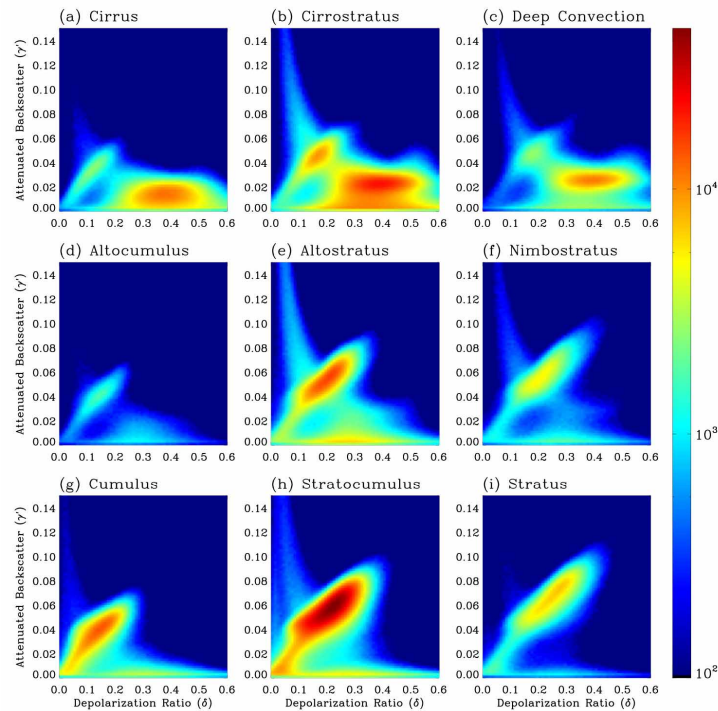


Fig. 2. The CALIPSO lidar  $\delta$ - $\gamma'$  relationships for nine ISCCP cloud types, as classified using MODIS data. Observations are over 12 months, from July 2006 to June 2007. The color of each pixel represents the frequency of occurrence for a  $\Delta\delta - \Delta\gamma'$  box with 0.01 by 0.002  $\text{sr}^{-1}$  interval.

The results in Fig. 2 show that many pixels correspond to small backscatter values that are likely caused by thin cirrus clouds or the uppermost thin clouds in the case of multi-layered clouds. MODIS cloud-height retrievals encounter difficulty in cases of optically thin clouds and multi-layered clouds [24,25]. According to Weisz et al. [26], there are relatively large differences between MODIS and CALIPSO cloud-top height retrievals, particularly for thin cirrus clouds. In the MODIS cloud top retrievals, very thin cirrus clouds (low  $\gamma'$  values) that are not detected by MODIS may be incorrectly classified as a cloud type associated with a lower layer. To avoid the potential ambiguity caused by mismatching cloud top retrievals and overlapping clouds in the cloud phase features shown in the CALIPSO  $\delta$ - $\gamma'$  relation, we screened both the MODIS and CALIPSO data to eliminate cases in which the CALIPSO lidar detected multi-layered clouds.

Cloud top heights of the uppermost CALIPSO layers were converted to pressures using the National Centers for Environmental Prediction (NCEP) re-analysis profiles interpolated to CALIPSO grids. Table 1 lists the mean pressure difference (MPD) and the standard deviation (SD) of the differences between the cloud top pressures obtained from MODIS and CALIPSO during the daytime in August 2006. The quantities MPD and SD are defined as follows:

$$\text{MPD} = \frac{1}{N} \sum_{i=0}^N (P_{i,\text{MODIS}} - P_{i,\text{CALIPSO}}), \quad (3)$$

and

$$\text{SD} = \sqrt{\frac{1}{N-1} \sum_{i=0}^N ((P_{i,\text{MODIS}} - P_{i,\text{CALIPSO}}) - \text{MPD})^2}, \quad (4)$$

respectively. In Eqs. (3) and (4),  $N$  indicates the total number of the pixels. It is evident from Table 1 that the screened data sets show a smaller MPD and SD values in comparison with the unscreened case.

Table 1. Statistics of the differences between the MODIS and CALIPSO cloud-top pressure retrievals.

	Number of Pixels	MPD (hPa)	SD (hPa)
Uppermost layers	5429675	67.2	170.2
Single-layers	3772072	29.5	155.4

Figure 3 shows the histograms of the difference between the MODIS and CALIPSO cloud height retrievals in terms of cloud-top pressure difference. The left panel shows the histogram in terms of number of pixels versus the cloud-top pressure difference. Because the unscreened case has more pixels than the screened case (see Table 1), the histogram curve of the unscreened case is higher than of the screened case. The right panel shows the normalized frequency of the distribution of the difference between the MODIS and CALIPSO cloud height retrievals. Here the normalized frequency is defined as the ratio of the number of pixels in each histogram bin shown in the left panel of Fig. 3 to the number of total pixels involved in the statistics. The right panel of Fig. 3 shows that the peak of the curve is located at  $P_{\text{MODIS}} - P_{\text{CALIPSO}} \approx 10$  hPa in the screened case whereas the peak of the normalized frequency in the unscreened case is shifted to  $P_{\text{MODIS}} - P_{\text{CALIPSO}} \approx 30$  hPa. While, the normalized frequencies in the screened and unscreened cases look quite similar, it is clear that the MODIS results agree better with the CALIPSO retrievals in the case of single-layered clouds than in the unscreened case where multi-layered clouds exist.

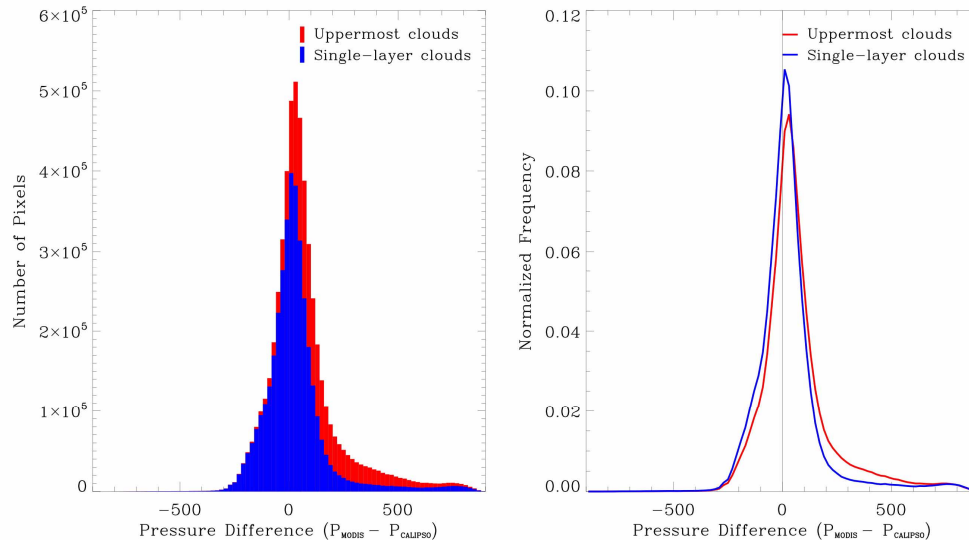


Fig. 3. Histogram and normalized frequency of the difference between the MODIS and CALIPSO cloud top pressure retrievals during daytime in the August of 2006.

As the screened counterpart of Fig. 2, Fig. 4 shows the  $\delta$ - $\gamma'$  relations for global single-layered clouds. Overall, the features shown in the  $\delta$ - $\gamma'$  relations in the screened (Fig. 4) and unscreened (Fig. 2) cases are similar. However, the major difference between the results shown in Figs. 2 and 4 is that small values of attenuated backscatter are eliminated for both water and ice features in the screened case, particularly for moderate and thick clouds. As already explained, small backscatter may be due to the presence of multi-layered clouds containing thin uppermost layers that MODIS does not detect. It is evident from Fig. 4 that weak features associated with thin ice layers (i.e., pixels with low  $\gamma'$  values) are still observed in cumulus and stratocumulus classes.

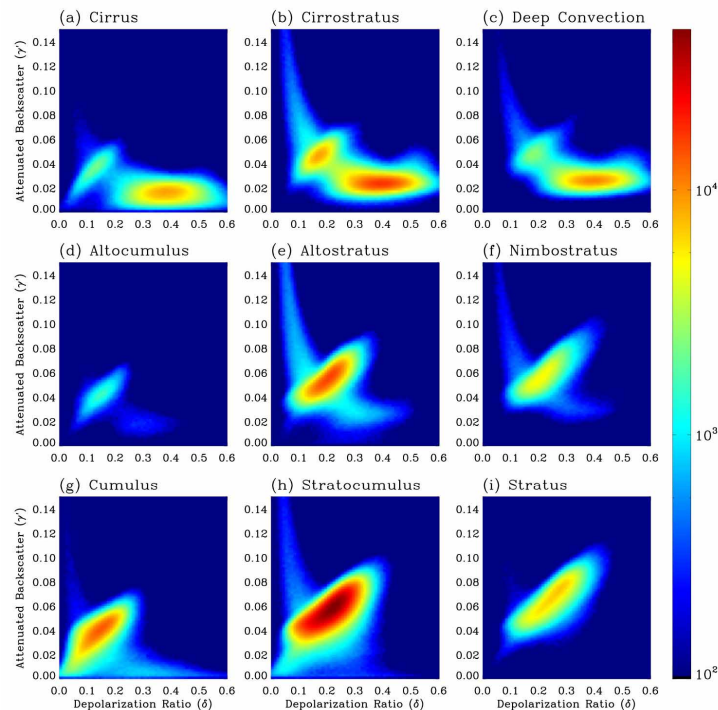


Fig. 4. Same as Fig. 2 except for single-layer clouds identified from the CALIPSO data.

To investigate the dependence of the cloud  $\delta$ - $\gamma'$  relationship on geographic location, we investigate the  $\delta$ - $\gamma'$  relationship for three latitude regimes: tropics (30°S to 30°N), midlatitudes (30°N to 60°N and 30°S to 60°S), and high latitudes (60°N to 90°N and 60°S to 90°S). The complete dataset, unscreened for multiple cloud layers, is used for the geographic analysis. The results for the tropical region are shown in Fig. 5. In the tropical region only water phase features are observed for low and middle clouds; however, both water and ice features with patterns quite similar to those shown in the high cloud classes in Fig. 2 are observed in the case of tropical high clouds. Horizontally oriented crystals are present only in the cirrostratus cloud class. The majority of the tropical high cloud observations show signatures of randomly oriented ice crystals with depolarization ratios between 0.3-0.5. *In situ* observations of tropical ice clouds show that the shapes of ice crystals within tropical ice clouds, especially those associated with strong deep convection, can be complicated and irregular [27]. Irregular ice crystal shapes would lead to high depolarization ratios and low backscatter values, which could explain the absence of an oriented crystal signature in Fig 5 except for the cirrostratus class.

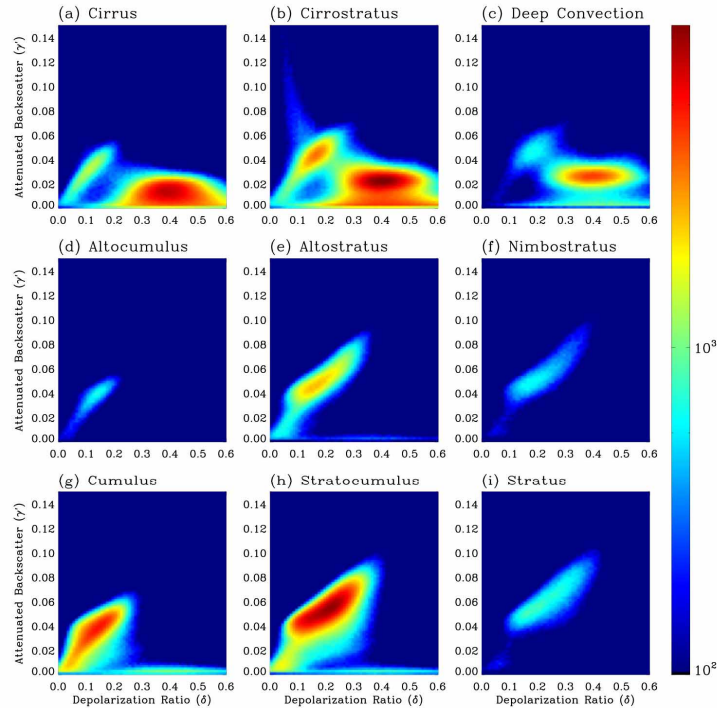


Fig. 5. The  $\delta$ - $\gamma'$  relations for nine cloud types in the tropical region from 30°S to 30°N.

The  $\delta$ - $\gamma'$  relations for the midlatitude regime are shown in Fig. 6. For the midlatitude cases, ice signatures are seen in all the cloud classes except for stratus; water signatures are seen in all of the classes. Signatures corresponding to horizontally oriented ice crystals are found more often in the midlatitude cases than in the tropics, and are strongest in the moderate optical thickness classes. Differing from the tropical cloud systems shown in Fig. 5, both water and ice phases are observed in midlatitude mid-level clouds. The lack of ice feature in the mid-level tropics may be explained by different temperature ranges according to latitude bands. A pressure range of mid-level (440 to 680 hPa) in the midlatitude will cover lower temperature ranges than in the tropics, so the mid-level clouds in the midlatitude regions might contain more ice phase crystals. Additionally, the ice-phase feature is also weakly shown in the  $\delta$ - $\gamma'$  relationship for the midlatitude nimbostratus and stratocumulus cloud classes. Furthermore, it is evident from Fig. 6 that horizontally oriented ice crystals are present in midlatitude cirrostratus, deep convection, altostratus, nimbostratus, and stratocumulus classes. Pristine ice crystals have been observed in the midlatitudes by aircraft or balloon-borne instruments (e.g., Heymsfield and Iaquinta [28]). If pristine ice plates or columns are horizontally oriented, the corresponding depolarization ratios are low. The existence of ice and water cloud signatures in the midlevel cloud classes may point to mixed-phase clouds, which occur frequently in the midlatitudes [20,22,29], and/or separate cases of water phase and ice phase clouds.

The  $\delta$ - $\gamma'$  relations for the polar regions are shown in Fig. 7. Overall, the patterns shown in Figs. 6 and 7 are quite similar. However, the high cloud classes, especially the deep convection class, occur less frequently in the polar regions than in the tropics and midlatitudes. Both water and ice signatures are found in all of the polar classes except for the stratus and cumulus classes. The cirrostratus class has the largest fraction of ice signature, most of which is randomly oriented. Similar to the midlatitude case, all of the moderate optical thickness classes demonstrate the oriented crystal feature. It should be pointed out that the polar region MODIS cloud classes may have more errors than the tropical and midlatitude

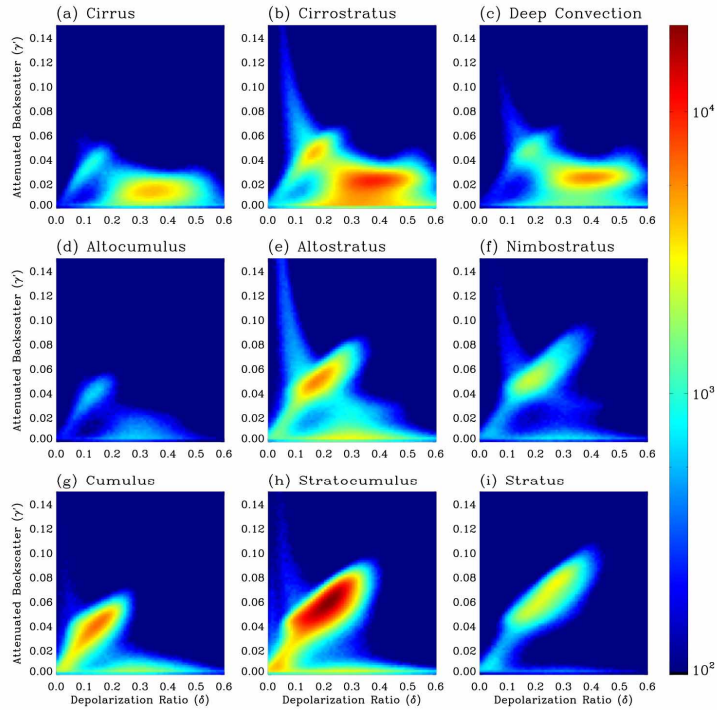


Fig. 6. The  $\delta$ - $\gamma'$  relation for nine cloud types in the midlatitudes (30°S-60°S and 30°N-60°N).

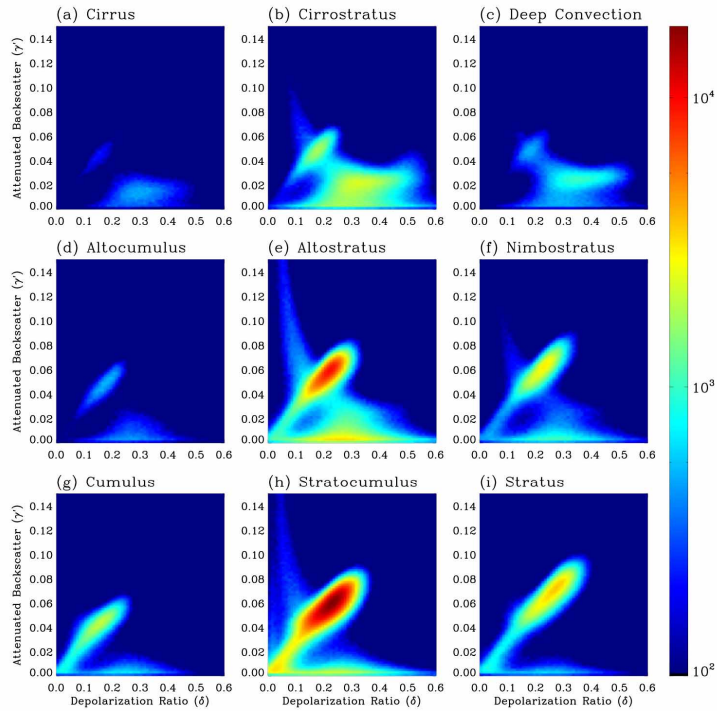


Fig. 7. The  $\delta$ - $\gamma'$  relationships for clouds in the polar regions (60°S-90°S and 60°N-90°N).

classes due to the difficulties in MODIS cloud detection and cloud property retrieval over cold, bright surfaces with low solar elevation angles.

We consider the relationship between cloud thermodynamic phase and cloud top temperature in Figure 8. The  $\delta$ - $\gamma'$  relations from CALIPSO are shown for nine MODIS cloud top temperature retrieval ranges. As expected, the clouds with cloud-top temperatures above 0°C correspond mainly to the water cloud feature in the  $\delta$ - $\gamma'$  relation, whereas the clouds with cloud top temperatures below -45°C correspond primarily to the feature associated with randomly oriented ice crystals. However, water features are observed for cloud-top temperatures as cold as -45°C and ice features are noticed for cloud-top temperatures as warm as -5°C. For cloud top temperatures between -5°C and -25°C, the observed ice features correspond to horizontally oriented ice crystals, while both oriented and non-oriented crystal features are seen between -25° and -40°C. Within these temperature ranges, ice crystals and supercooled water drops can occur in single-phase or mixed-phase clouds. An interesting feature is the apparent increase in depolarization ratio with decreasing temperature for randomly oriented ice crystals. The differences between MODIS and CALIPSO retrieved cloud height, especially in the case of thin clouds, may impact these results, as the MODIS cloud top temperatures are inferred from the cloud top pressure retrievals for midlevel and upper level clouds.

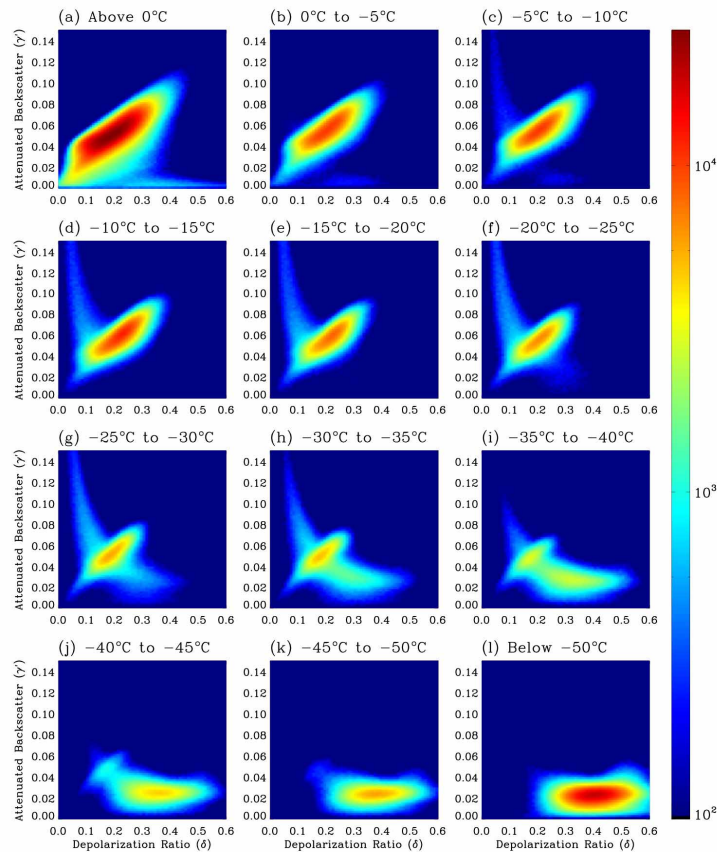


Fig. 8. The  $\delta$ - $\gamma'$  relationships with respect to cloud top temperature obtained by MODIS cloud retrievals for single-layer clouds identified from the CALIPSO data.

The CALIPSO lidar measurements are an independent source of information about cloud phase that can be compared against the two MODIS-derived cloud phase products described

in Section 2. The MODIS bispectral IR cloud phase algorithm results are shown in Figs. 9-11, while those from the RPP phase algorithm are shown in Figs. 12-14. The global  $\delta$ - $\gamma'$  relations for all clouds identified as water phase by the operational MODIS bispectral IR algorithm are shown in Fig. 9. In this case, high frequencies of occurrence are observed for the three low cloud classes, as well as two of the middle cloud classes, altostratus and nimbostratus. Comparisons with Fig. 2 show that the clouds causing the strong water cloud signatures in the upper level clouds in the entire dataset are not being classified as water by the MODIS IR phase algorithm. There is, however, a weak component of the cirrus class exhibiting a randomly oriented crystal lidar signature that is classified as water by MODIS. Fig. 9 shows that the vast majority of clouds classified as water by the MODIS phase algorithm exhibit  $\delta$ - $\gamma'$  signatures associated with water clouds.

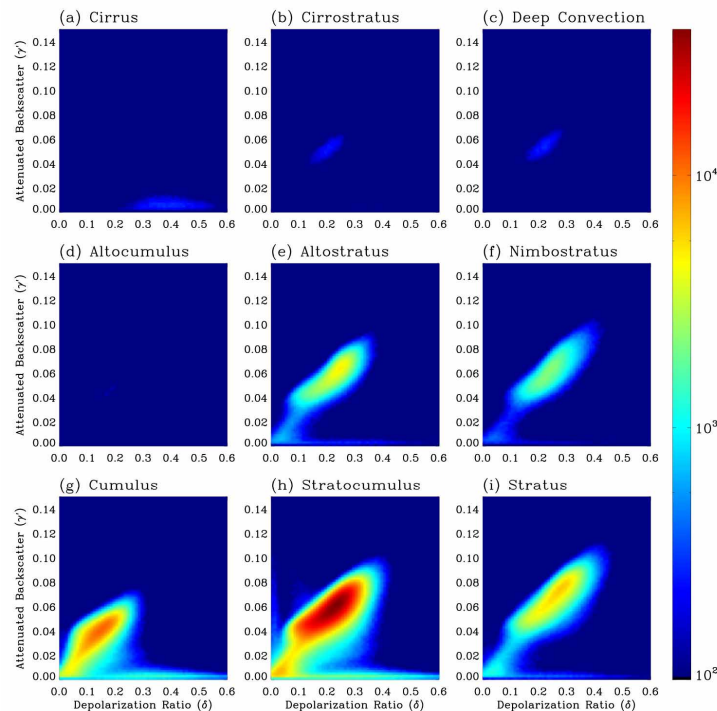


Fig. 9. The  $\delta$ - $\gamma'$  relationships for the clouds flagged as in water-phase by the MODIS IR cloud-phase determination algorithm [12].

Figure 10 shows the global  $\delta$ - $\gamma'$  relations for clouds identified as ice phase by the MODIS IR-phase algorithm. The most obvious feature is that the low cloud classes are not populated. Strong lidar signatures associated with randomly oriented crystals are seen in the high cloud classes, and, to a lesser extent, in the altostratus class. However, the typical water-phase  $\delta$ - $\gamma'$  feature is observed in the alto cumulus, altostratus, cirrus and cirrostratus classes. These water features may mean that MODIS misclassified some water clouds as ice. There are other possibilities, including mixed-phase clouds, or heterogeneous cloud features (i.e., the co-existence of ice clouds and water clouds) within the MODIS phase 5 km x 5 km footprint.

Figure 11 shows the global  $\delta$ - $\gamma'$  relations for those clouds identified as mixed and unknown phase by the MODIS IR algorithm. The greatest number of MODIS pixels with this classification fall into the cirrostratus, altostratus, stratocumulus, nimbostratus, and deep convection classes, and both water and ice features are seen in the  $\delta$ - $\gamma'$  relations. This is not surprising as the MODIS IR algorithm assigns mixed or unknown phase to clouds with spectral and thermal signatures that do not definitively point to either ice or water phase. Comparisons of Fig. 11 to Fig. 10 show that clouds exhibiting features associated with

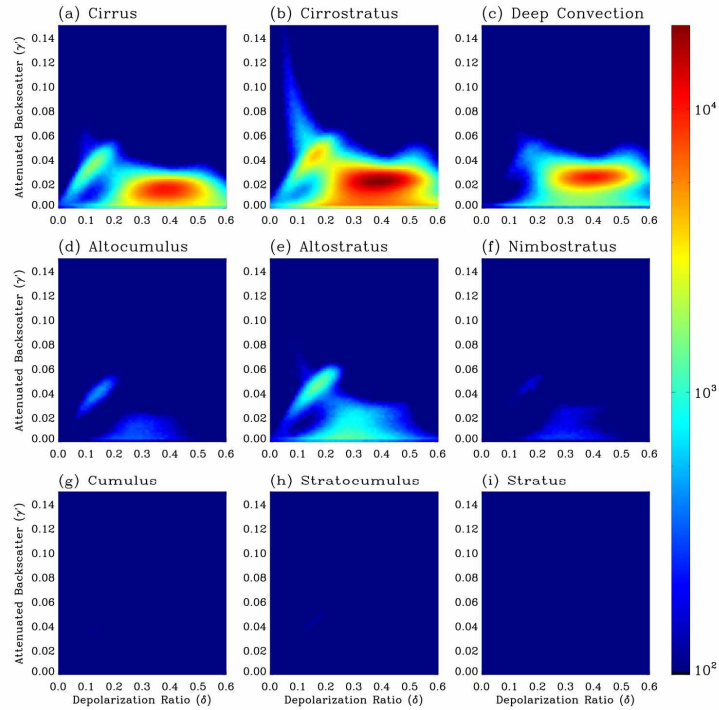


Fig. 10. The  $\delta$ - $\gamma'$  relationship for the clouds flagged as in ice-phase by the MODIS IR cloud-phase determination algorithm [12].

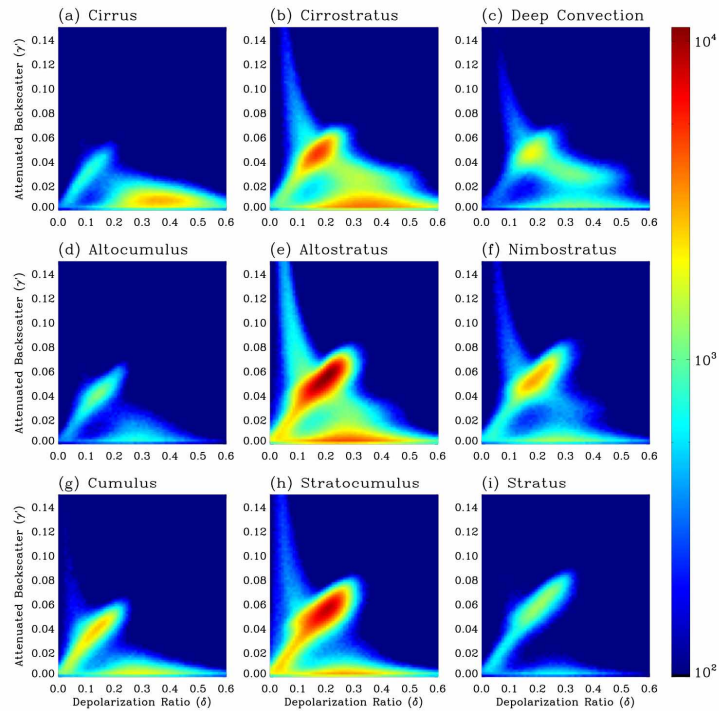


Fig. 11. The  $\delta$ - $\gamma'$  relationship for clouds flagged as in mixed- or uncertain-phase by the MODIS IR cloud-phase determination algorithm.

horizontally-oriented ice crystals are likely to be classified as mixed or unknown phase by MODIS. This tendency warrants further study.

The  $\delta$ - $\gamma'$  relations for water, ice, and undetermined phase classifications, based on the MODIS cloud property retrieval processing path (RPP) phase algorithm are shown in Figs. 12-14. The RPP phase algorithm utilizes a number of visible, near-infrared, and infrared MODIS channels, but can only be applied to daytime MODIS observations. Fig. 12 shows the  $\delta$ - $\gamma'$  relations for those clouds classified as water by the RPP. The majority of the clouds classified as water by the RPP demonstrate features indicative of water in the lidar relations, although randomly oriented crystal features are seen in the cirrus and cirrostratus classes, and weak features associated with horizontally oriented particles are seen in the moderate optical thickness classes. This feature is not seen in the MODIS IR phase plot, implying that the IR phase algorithm classifies these scenes as having mixed or unknown phase.

The clouds classified as ice by the MODIS RPP are shown in Fig. 13. The  $\delta$ - $\gamma'$  relations for the upper level clouds look similar to those for the MODIS IR phase plot in Fig. 10. The midlevel cloud features indicative of water clouds are stronger in the MODIS RPP ice case, though, and some low level clouds with water features are classified as ice by the MODIS RPP. More detailed case studies are necessary to understand these features. An interesting note is that the RPP algorithm classifies a much larger fraction of the horizontally-oriented crystal features as ice than does the IR phase algorithm, which tends to classify them as mixed or unknown.

Only a small fraction of the RPP cases are classified as undetermined phase. The  $\delta$ - $\gamma'$  relations in Fig. 14 show that the midlevel and low level undetermined clouds tend to demonstrate strong water features, while the cirrus class shows moderate ice features. Several classes, cirrostratus, deep convection, and altocumulus, are basically unpopulated.

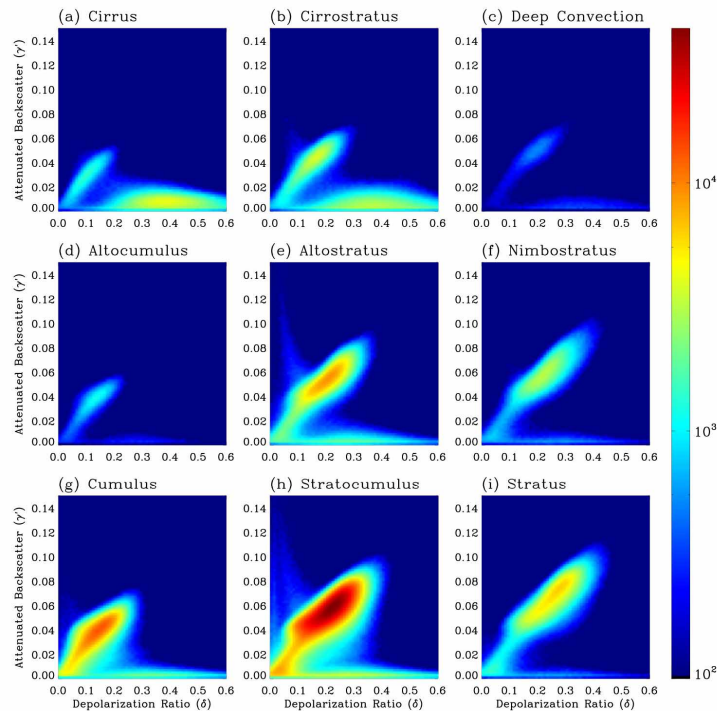


Fig. 12. The  $\delta$ - $\gamma'$  relationship for clouds flagged as water-phase by the MODIS cloud property retrieval processing path (RPP) phase determination algorithm.

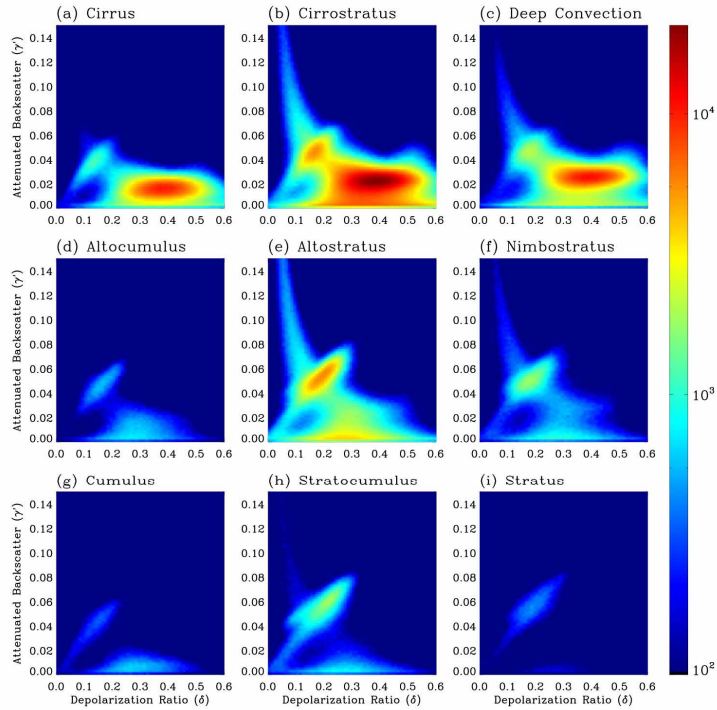


Fig. 13. The  $\delta$ - $\gamma$  relationship for clouds flagged as ice-phase by the MODIS RPP phase determination algorithm.

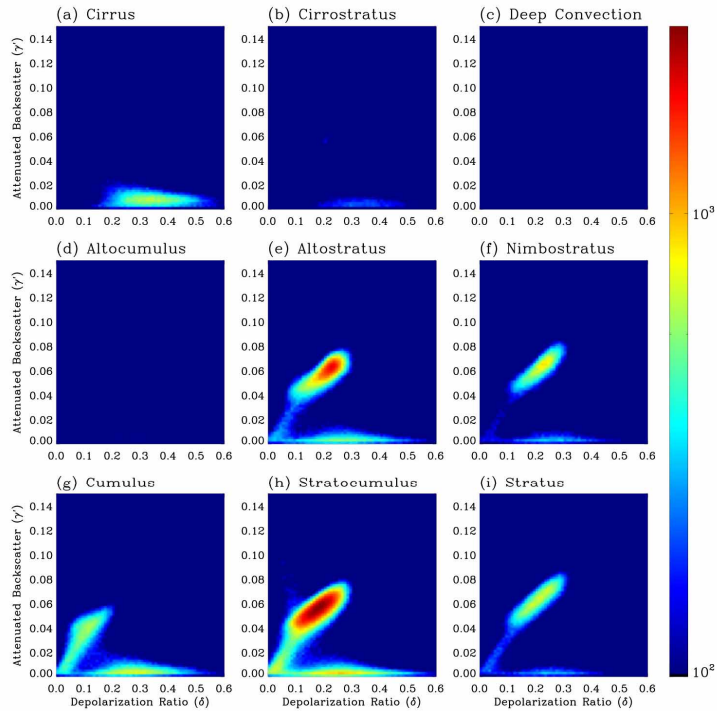


Fig. 14. The  $\delta$ - $\gamma$  relationship for clouds flagged as undetermined-phase by the MODIS RPP phase determination algorithm.

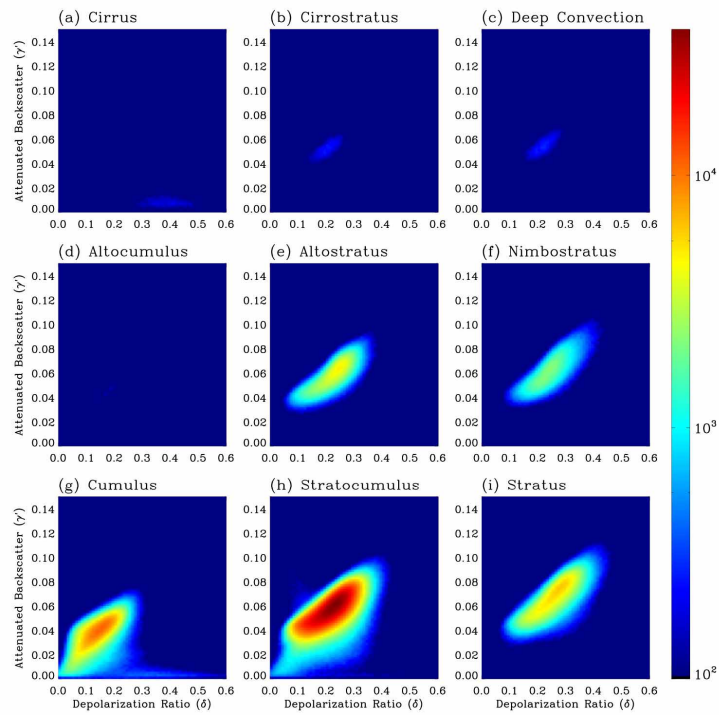


Fig. 15 Same as Fig. 9 except for single-layer clouds identified from the CALIPSO data.

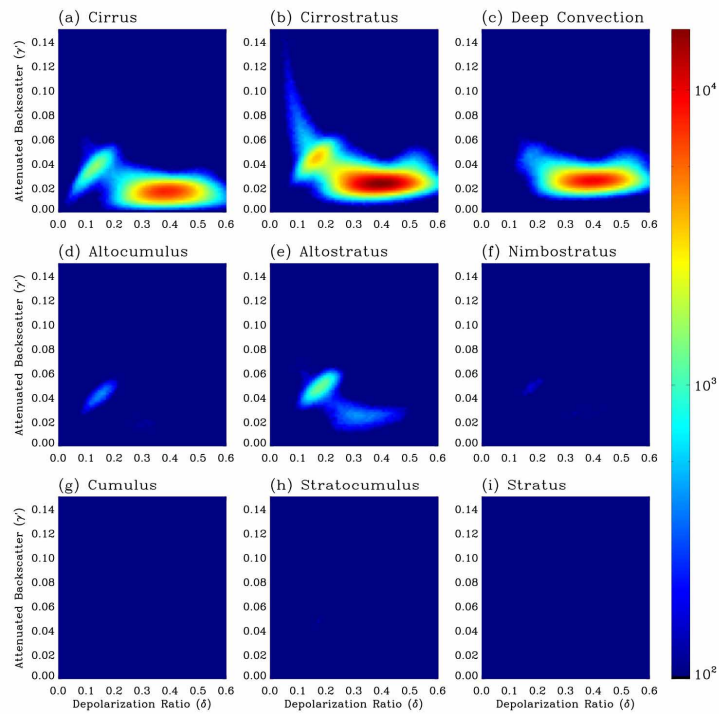


Fig. 16. Same as Fig. 10 except for single-layer clouds identified from the CALIPSO data.

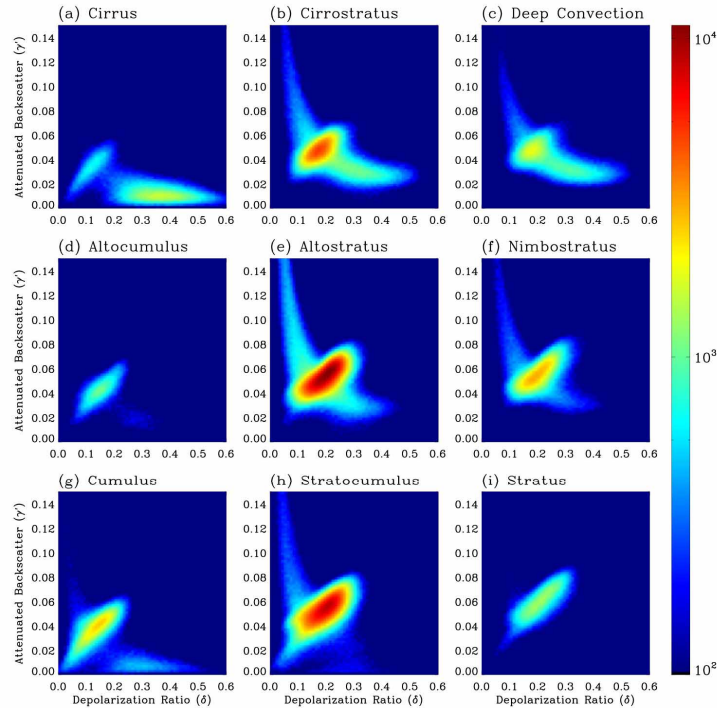


Fig. 17. Same as Fig. 11 except for single-layer clouds identified from the CALIPSO data.

Figures 15, 16 and 17 show the  $\delta$ - $\gamma'$  relations for single-layered water, ice, and mixed-/uncertain-phase clouds, respectively, which are identified on the basis of the MODIS bispectral IR phase algorithm. The unscreened counterparts of Figs. 15, 16 and 17 are Figs. 9, 10 and 11, respectively. Again, the overall features in the  $\delta$ - $\gamma'$  relations shown in the screened and unscreened cases are similar; however, low  $\gamma'$  values associated with the uppermost thin clouds are eliminated in the screened results. Furthermore, it seems likely, based on comparison of Figs. 17 and 11, that many clouds identified as mixed- or uncertain-phase by the MODIS IR algorithm have more than one layer.

#### 4. Summary

We investigated the relationships between layer-averaged depolarization ratio ( $\delta$ ) and layer-averaged attenuated backscatter ( $\gamma'$ ) measured by the CALIPSO lidar for nine ISCCP cloud classes. The CALIPSO lidar contains information on up to 10 cloud layers within each 1 km retrieval footprint; however only the uppermost cloud layer is considered in this study. The cloud class assignment was made on the basis of the MODIS retrievals of cloud-top pressure and cloud optical depth for a period of 12 months from July 2006 to June 2007. Because of the dependence on MODIS optical depth retrievals, only daytime observations are included in the study. On a global scale, the CALIPSO lidar  $\delta$ - $\gamma'$  relation associated with water clouds is observed for all nine cloud types. The  $\delta$ - $\gamma'$  feature associated with horizontally oriented ice crystals is prominent for cirrostratus, deep convection, altostratus, and nimbostratus classes. Furthermore, we screened both the MODIS and CALIPSO data to eliminate the cases in which two or more cloud layers were observed. It is shown that very low  $\gamma'$  values in the unscreened case were largely eliminated in the case of single-layered clouds. These low  $\gamma'$  values correspond to the uppermost thin layers in two- or multi-layered cloud systems.

The dependence of the  $\delta$ - $\gamma'$  relation on latitude was also considered. For the tropical region (30°S-30°N), only the water-phase feature is observed in the CALIPSO lidar  $\delta$ - $\gamma'$  relation for low and mid-level clouds; however, both water-phase and ice-phase signatures are observed for high clouds. In the midlatitude and polar regions, both water-phase and ice-

phase are observed for high and middle clouds. Additionally, the feature associated with horizontally oriented ice crystals is prominent for cirrostratus and altostratus clouds. In addition to the analysis of the CALIPSO lidar  $\delta-\gamma'$  relation for cloud systems at three latitude belts, we also analyzed the lidar  $\delta-\gamma'$  relations for various cloud top temperatures. Randomly oriented ice crystal features correspond to colder cloud top temperatures than horizontally oriented crystals. Additionally, the depolarization ratio associated with randomly oriented ice crystals increases for colder cloud top temperatures.

We investigated the CALIPSO lidar  $\delta-\gamma'$  relationship with respect to the cloud phase determined from both the operational MODIS bi-spectral infrared phase algorithm and the MODIS cloud optical properties retrieval processing path phase algorithm. It is shown that the MODIS bi-spectral IR algorithm is consistent with that indicated by the CALIPSO lidar  $\delta-\gamma'$  relationship for water clouds. However, the typical feature associated with water phase in the  $\delta-\gamma'$  relationship is observed for the clouds that are identified as ice by the MODIS IR algorithm. Both water and ice signatures are observed for those clouds classified as mixed or unknown phase by the MODIS IR algorithm. On the other hand, the RPP algorithm misclassifies a lot of ice clouds as water clouds (Figs. 12-13). Although the MODIS IR algorithm is generally more conservative in its phase classification for most cloud systems, the RPP algorithm is more effective in detecting ice clouds consisting of horizontally oriented ice crystals, as evident from a comparison of Figs. 10 and 13. The present results clearly demonstrate the unique capabilities of the CALIPSO lidar instrument for determining cloud phase.

### **Acknowledgements**

Ping Yang's research is supported by the National Science Foundation Physical Meteorology Program (ATM-0239605), and a research grant (NNL06AA23G) from the National Aeronautics and Space Administration (NASA). George Kattawar's research is supported by the Office of Naval Research under contracts N00014-02-1-0478 and N00014-06-1-0069. Patrick Minnis is supported through the NASA Radiation Sciences Program and the NASA Clouds and the Earth's Radiant Energy System Project.